Journal of Power Sources 378 (2018) 499–510

Contents lists available at ScienceDirect

Journal of Power Sources

journal homepage: www.elsevier.com/locate/jpowsour

Pomelo peels-derived porous activated carbon microsheets dual-doped with nitrogen and phosphorus for high performance electrochemical capacitors

Zhen Wang[b], Yongtao Tan[a,b], Yunlong Yang[b], Xiaoning Zhao[b], Ying Liu[a,b], Lengyuan Niu[c], Brandon Tichnell[d], Lingbin Kong[a,b], Long Kang[a,b], Zhen Liu[d], Fen Ran[a,b,*]

[a] State Key Laboratory of Advanced Processing and Recycling of Non-ferrous Metals, Lanzhou University of Technology, Lanzhou 730050, PR China
[b] School of Material Science and Engineering, Lanzhou University of Technology, Lanzhou 730050, Gansu, PR China
[c] Institute of Coordination Bond Metrology and Engineering, College of Materials Science and Engineering, China Jiliang University, Hangzhou 310018, PR China
[d] Department of Physics & Engineering, Frostburg State University, Frostburg, MD 21532-2303, USA

HIGHLIGHTS

- Porous activated carbon nanosheets fabricated by biowaste mass of pomelo peels.
- Dual-doped with nitrogen and phosphorus elements by using ammonium phosphate.
- High specific surface area of 807.7 m^2/g and large pore volume of 0.4378 cm^3/g.
- A capacitance of 240 F/g with 100% of capacitance retention after 10,000 cycles.
- Symmetric electrochemical capacitor device exhibits an energy density of 11.7 Wh/kg.

GRAPHICAL ABSTRACT

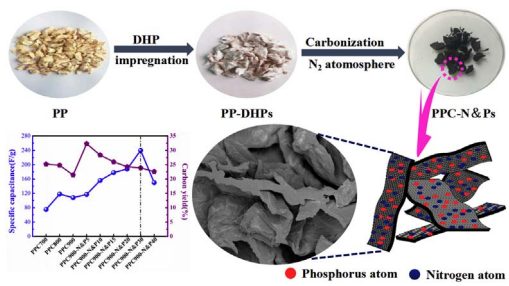

ARTICLE INFO

Keywords:
Biomass
Carbon material
N&P-doping
Electrochemical capacitor
Porous structure

ABSTRACT

In this work, biomass pomelo peel is used to fabricate the porous activated carbon microsheets, and diammonium hydrogen phosphate (DHP) is employed to dual-dope carbon with nitrogen and phosphorus elements. With the benefit of DHP inducement and dual-doping of nitrogen and phosphorus, the prepared carbon material has a higher carbon yield, and exhibits higher specific surface area (about 807.7 m^2/g), and larger pore volume (about 0.4378 cm^3/g) with hierarchically structure of interconnected thin microsheets compared to the pristine carbon. The material exhibits not only high specific capacitance (240 F/g at 0.5 A/g), but also superior cycling performance (approximately 100% of capacitance retention after 10,000 cycles at 2 A/g) in 2 M KOH aqueous electrolyte. Furthermore, the assembled symmetric electrochemical capacitor in 1 M Na_2SO_4 aqueous electrolyte exhibits a high energy density of 11.7 Wh/kg at a power density of 160 W/kg.

1. Introduction

Since the early 1950s, there has been significant attention on the development of electrochemical capacitors due to their high charging and discharging efficiency, long cycle life, and high power density. [1–3]. The electrode material is an important component of electrochemical capacitors, including carbon material [4,5], transition metal oxide/nitride (such as NiO, VN [6,7]), and a conductive polymer [8].

* Corresponding author. State Key Laboratory of Advanced Processing and Recycling of Non-ferrous Metals, Lanzhou University of Technology, Lanzhou 730050, PR China.
E-mail addresses: ranfen@lut.cn, ranfen@163.com (F. Ran).

https://doi.org/10.1016/j.jpowsour.2017.12.076
Received 31 August 2017; Received in revised form 5 December 2017; Accepted 26 December 2017
Available online 04 January 2018
0378-7753/

The metal oxide/nitride and conductive polymer provide a large pseudocapacitance, but the cycle stability is poor [9]. In contrast, carbon materials have excellent electrical properties, good physical and chemical stability, and high specific surface area, and thus they are currently the most commonly used electrode materials of electrochemical capacitors. Nowadays, there are some novel routes for fabricating electrode materials, such as crystal-structure modification [10], heterostructured nanocomposites [11], experimental, simulation-based [12], and so on. In addition, a study on C/Si_3N_4 composites [13] and some other applications of the materials such as capacitor, intelligent sensor [14–17] have been proposed, which further expanded the application of carbon composites materials.

The material sources for the preparation of carbon materials are quite extensive, such as polymers [18,19], which expand the usage of recycled polymers for multifunctional nanocomposites preparation with various fillers [20–22] and different hosting polymer matrices [23–26]. Due to the shortage of fossil resources such as oil and coal, the use of waste biomass sources prepared carbon materials for energy applications, have become the focus of researchers due to the low cost and environment-friendly properties. There are many works that have utilized various waste biomass to derive carbon materials, such as fungi [27], pistachio shells [28], banana peels [29,30], cassava peels [31], seaweed [32], firewood [33], and so on, which have exhibited excellent electrochemical properties as electrode materials for electrochemical capacitors. In comparison, the pomelo peel is a widely distributed biomass precursor material. Up to now, there are some reports have utilized the abandoned pomelo peel to synthesize carbon materials by KOH activation for energy applications [34–36]. The prepared carbon materials have a high specific surface area, however, the yield of carbon materials is always ignored in these works. Furthermore, the research showed that cellulose was a linear homopolymer of the glucopyranose residue linked by the β-1, 4-glycosidic linkage, which was the most important component of the biomass [37]. It was confirmed that levoglucan was the main product in the cellulose pyrolysis process (accounting for more than 50% by weight), and it was easy to volatilize at high temperatures [38]. Hence, it needs to be pointed out that the carbon yield was crucial for utilized various waste biomass to derive carbon materials. Recently, some reports showed that addition of acid would inhibit the formation of levoglucose during the pyrolysis process [39,40].

In this work, we used the biomass pomelo peel to prepare porous activated carbon microsheets and used diammonium hydrogen phosphate (DHP) to introduce dual-doping of nitrogen and phosphorus via one-step carbonization under N_2 atmosphere. The decomposition of DHP could cause phosphorylation reactions [41] in pyrolysis process, which can effectively reduce the formation of levoglucose and enhance the formation of char [40]. Therefore, the carbon yield could be effectively improved. Meanwhile, the prepared carbon material would exhibit high specific surface area and uniform pore size distribution due to the inducement of the DHP-incorporated carbonization. Furthermore, DHP is an inorganic salt containing abundant nitrogen and phosphorus elements, which could effectively dope the carbon framework with nitrogen and phosphorus atoms. Which would largely improve the wettability of the carbon-based material in the aqueous electrolytes. Therefore, as the electrode material of electrochemical capacitors, the prepared carbon microsheets would exhibit good electrochemical performance.

2. Experimental

2.1. Chemicals and materials

Pomelo peel (PP) was recycled from pomelo after being washed with the mixed solvent of deionized water and alcohol and dried under vacuum at 60 °C overnight. Diammonium hydrogen phosphate (DHP) of analytical grade was purchased from *Sinopharm Chemical Reagent Co. Ltd.*

2.2. Preparation of dual-doped carbon

i) In a typical synthesis, the obtained dry PP (4 g) was heat-treated under N_2 atmosphere in a tube furnace at the temperatures of 700–900 °C for 2 h in a flow of 70 sccm (the abbreviation of standard cubic centimeter per minute). Then the sample was naturally cooled down to room temperature to obtain normal carbon material.
ii) For further modification, the dry PP (4 g) was treated with DHP aqueous solution for 24 h, followed by wringing and then drying under a vacuum at 60 °C for 48 h. The DHP treated pomelo peel was heat-treated at 900 °C for 2 h in a tube furnace with an N_2 flow of 70 sccm. Finally, the dual-doped porous activated carbon was fabricated. The ratio of the remaining carbon of the samples was calculated according to the following equation:

$$r_{\text{carbon}}\ (\%) = W_b/W_a \times 100\% \quad (1)$$

Where W_b (g) is the quality of final samples after carbonization, and W_a (g) is the quality of pomelo peel after being washed and vacuum dried.

2.3. Materials structural characterization

The morphology and microstructure of the fabricated materials were characterized using a HITACHI S-4800 scanning electron microscope (SEM) and transmission electron microscope (TEM, JEOL, JEM-2010, Japan). The X-ray photoelectron spectroscope (XPS, physical Electronics UK) was used to analyze the chemical composition of the samples. The Raman spectroscopy (Horiba Scientific, France, excitation-beam wavelength = 532 nm) was used to characterize the properties of materials. The specific surface area and pore structure of the samples was characterized by Nitrogen adsorption and desorption experiments at 77 K (Micromeritics, ASAP 2010M,USA). The specific surface area was calculated from the nitrogen adsorption isotherm using Brunauer-Emmett-Teller (BET) method and the Non Local Density Functional Theory (NLDFT) model was used to analyze the pore size distribution of samples.

2.4. Electrochemical performance

The working electrodes that were used for electrochemical measurements were prepared as follows: the fabricated carbon samples, carbon black, conductive graphite, and PTFE were mixed at a weight ratio of 80: 7.5: 7.5: 5 to make a homogeneous black paste and then coated on the surface of nickel foam, which was used as a current collector. The electrode was dried under vacuum at 60 °C for 6 h, and compressed at a pressure of 10 MPa to minimize the loss of electroactive materials during the electrochemical testing process. The performance of electrochemical properties was tested using cyclic voltammetry (CV), galvonostatic charging-discharging (GCD) and electrochemical impedance spectroscopy (EIS) in an electrochemical workstation (CHI660E, Shanghai, China). The cycling stability test was performed using LAND CT2001A instrument.

*Regarding the Single Electrodes Test:*Electrochemical measurement was conducted at room temperature in a traditional three-electrode configuration containing the working electrode, a platinum gauze counter electrode, and a saturated calomel reference electrode. The alkaline solution (2 M KOH) was used as the electrolyte for electrochemical tests. Cyclic voltammetry was recorded between −1.0 and 0 V at different scan rates from 5 to 100 mV/s. For galvonostatic charging-discharging measurement, the current densities were varied from 0.5 to 10 A/g within the same potential range as in cyclic voltammetry measurements. The electrochemical impedance spectroscopy spectrum was acquired with a frequency range from 10^{-2}–10^5 Hz.

Regarding the Symmetric Electrochemical Capacitor Test: The solid-

state two electrodes symmetric electrochemical capacitor was assembled with two pieces of the same electrodes, using 1 M Na_2SO_4 aqueous as an electrolyte. Cyclic voltammetry was recorded at different scan rates from 5 to 200 mV/s with a potential window ranging from 0 to 1.6 V. For galvanostatic charging-discharging measurements, the current densities were varied from 0.2 to 3 A/g within the same potential range as in cyclic voltammetry measurements. The electrochemical impedance spectroscopy spectrum was acquired with a frequency range from 10^{-2}–10^5 Hz. The cycling test was performed using LAND CT2001A instrument.

The specific capacitance of electrodes was calculated from the discharging curves at different current densities according to the following equation (2):

$$C = I \times t/(\triangle V \times m) \tag{2}$$

Where C (F/g) is the specific capacitance, I (A) is the constant discharging current, $\triangle t$ (s) is the discharge time, $\triangle V$ (V) is the voltage change during discharging (excluding the *IR* drop) and m (g) is the mass of active materials on one electrode.

The energy density of the device was calculated according to the following equation (3) [35]:

$$E\ (\mathrm{Wh/kg}) = C \times \triangle V^2/(2 \times 3.6) \tag{3}$$

The power density of the device was calculated according to the following equation (4) [35]:

$$P\ (\mathrm{W/kg}) = E \times 3600/\triangle t \tag{4}$$

Where E (Wh/kg) is the energy density of the device, P (W/kg) is the power density of the device, C (F/g) is the specific capacitance, $\triangle V$ (V) is the voltage change during the discharging process (excluding the *IR* drop) and $\triangle t$ (s) is the discharging time.

3. Results and discussion

Pomelo peel (PP) was heat-treated under N_2 atmosphere, and the temperature of heat-treatment would affect carbon yield, structure, and electrochemical performance of the carbon materials. The fabricated pomelo peels-derived carbon microsheets (PPCs) at the temperature of 700, 800, and 900 °C were denoted as PPC700, PPC800, and PPC900, respectively. As shown in Fig. 1 and Table S1 in Supporting Information, with an increase of carbonization temperature, the carbon yields of samples were decreased from 25.2 wt.% to 21.4 wt.%, due to the decomposition of cellulose within the pomelo peels to produce large amounts of volatile levoglucan [38], especially at an elevated carbonization temperature. For electrochemical performance, PPC800 exhibited the highest specific capacitance of 118 F/g, but PPC900 showed better electrochemical performance behavior (Fig. S1 in the Supporting Information). The PPC800 (exhibiting a size of ~10 nm) had lower specific surface area than that of PPC900 (exhibiting a size of ~2 nm), but showed higher specific capacitance at the low current density due to the ion migration related to the current density and the pore size of the electrode [42,43]. At the low current density, the micropores (1–2 nm) would fully contribute to the charge storage, but within which the ion diffusion and transfer was difficult [44], leading to the lower capacitance; the mesopores (5–50 nm) provided a more effective accessible surface area for ion transport/charge storage [45], thus presented the higher capacitance. Raman spectroscopies of PPCs were illustrated in Fig. S2 in the Supporting Information. A band at 1580 cm^{-1} (G band), which corresponded to the ordered carbon structure with sp^2 electronic configuration, and a characteristic peak at 1350 cm^{-1} (D band) was observed, representing the disordered/defective structure of carbon [46]. The degree of graphitization was usually estimated by the intensity ratio of D/G band (I_D/I_G), the larger I_D/I_G ratio indicated the lower graphitization degree. With increasing carbonization temperature, the I_D/I_G value of PPCs decreased from 1.06 to 0.97, indicating a higher degree of graphitization at higher carbonization temperature. And the results revealed that PPC900 contained a lower degree of graphitic carbon and a certain amount of disordered sections or defects. This property would be greatly beneficial to improve electrical conductivity and the electrochemical performance of carbon materials [47]. After an overall consideration and rational estimation of structure and specific capacitance, 900 °C was chosen as the heat-treatment temperature for this kind of carbonization.

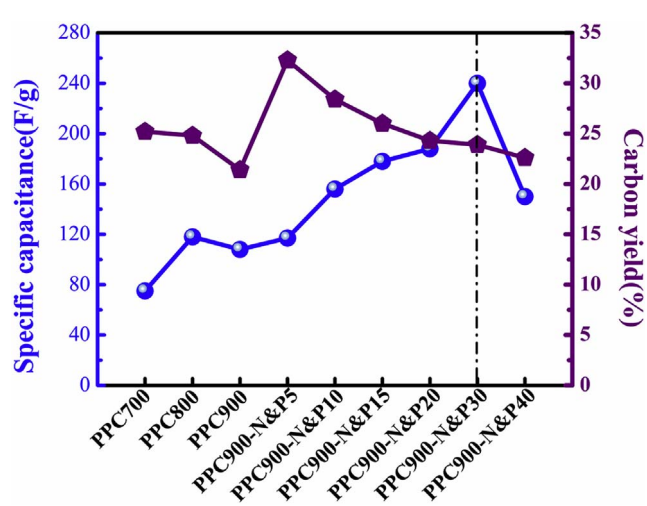

Fig. 1. The specific capacitance and carbon yield of samples.

Scheme 1 illustrated the preparation strategy of pomelo peels-derived porous activated carbon microsheets dual-doped with nitrogen and phosphorus elements (PPC-N&P). Compared to that of PPCs fabrication, DHP was incorporated to PP to form PP-DHPs intermediate as precursor for PPC-N&P. The dry PP was impregnated into DHP aqueous solution for 24 h, followed by wringing and then drying under vacuum at 60 °C for 48 h. The dry PP-DHPs were heated at 900 °C for 2 h in a tube furnace with an N_2 atmosphere. PPC-N&Ps prepared with the different mass fraction of 5, 10, 15, 20, 30, and 40 wt% DHP aqueous solution were named as PPC900-N&P5, PPC900-N&P10, PPC900-N&P15, PPC900-N&P20, PPC900-N&P30, and PPC900-N&P40, respectively. All carbon yields of DHP-incorporated samples were higher than that of PPC900 (Fig. 1 and Table S1 in the Supporting Information) because of the fact that DHP induced phosphorylation reactions in the pyrolysis process, which effectively reduced the formation of levoglucose. The formation of phosphoric acid at approximately 209 °C could be explained by the reactions of $(NH_4)_2HPO_4(s) \rightarrow NH_3(g) + NH_4H_2PO_4(s)$, $(NH_4)_2HPO_4(s) \rightarrow 2NH_3(g) + 4H_3PO_4(l)$, and $NH_4H_2PO_4(s) \rightarrow NH_3(g) + H_3PO_4(l)$, then the phosphoric acid was mainly dehydrated to produce pyrophosphoric acid by the reaction of $4H_3PO_4(l) \rightarrow 2H_2O(g) + 2H_4P_2O_7(l)$ at about 209 °C (DHP decomposition diagram according to the literature [41]). As the increase of DHP dosage, the carbon yield was gradually decreased from 32.3 wt% to 22.6 wt%, implying that DHP could protect the carbon skeleton. Refer to the electrochemical performance, the specific capacitance decreased with DHP increase, and PPC900-N&P30 exhibited the highest specific capacitance.

As shown in Fig. 2, PP exhibited dense flake morphology, and PPC900-N&P preserved the precursor's microstructure in great detail but demonstrated looser microsheet morphology. For PPC900 (Fig. S3 in the Supporting Information), there was no clear difference in the graphical morphologies; but it was obvious that PPC900-N&P possessed a looser arrangement, owing to the fact that DHP produced a lot of water vapor and NH_3 in the pyrolysis process [41], which increased the interlayer space and induced the large pore structure. As shown in Fig. 2d, the high-magnification image of PPC900-N&P displayed clearer microsheets character with many folds, and a uniform thickness of approximately 0.3 μm. Fig. 2e showed that the SEM elemental mapping

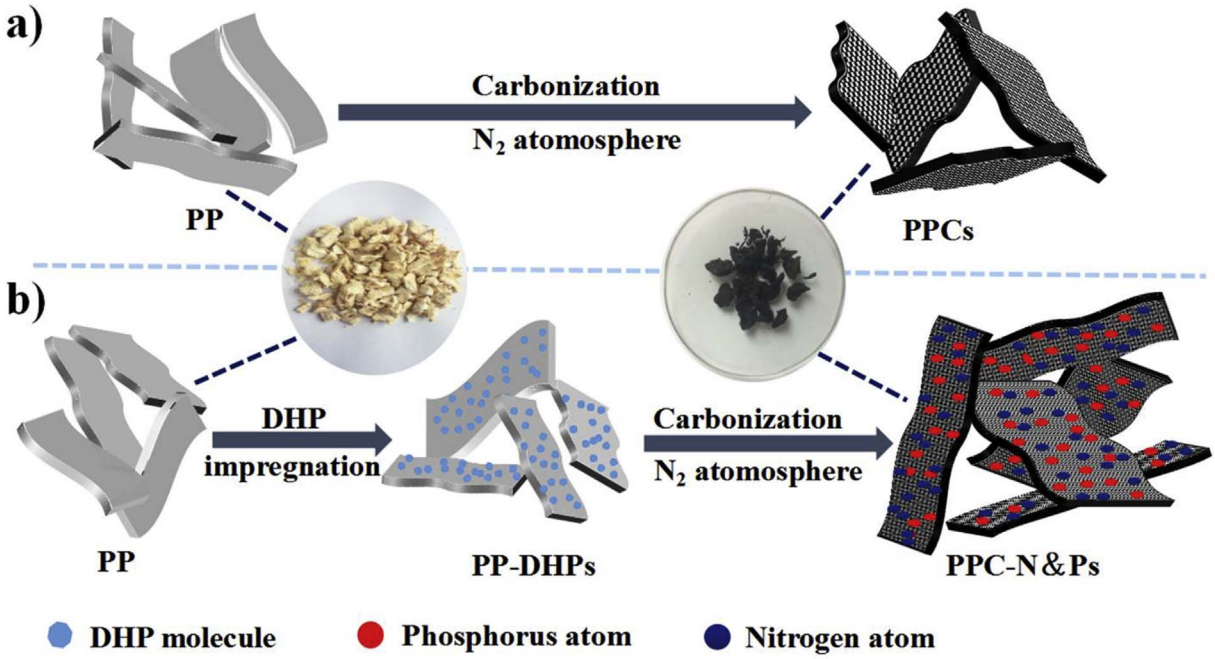

Scheme 1. Schematic illustration for the synthesis process of PPC-N&Ps.

images of PPC900-N&P: C, N, and P elements were homogeneously distributed in the matrix. From these results, it could be concluded that N and P atoms were efficiently doped into a carbon scaffold of PPC900-N&P.

The surface chemical composition of PPC900-N&P was further analyzed by XPS. As shown in Fig. 3a, the full XPS spectrum showed that the as-prepared carbon material mainly composed of C, N, P, and O elements. The peaks at 285, 400, 133, and 520 eV in full spectra

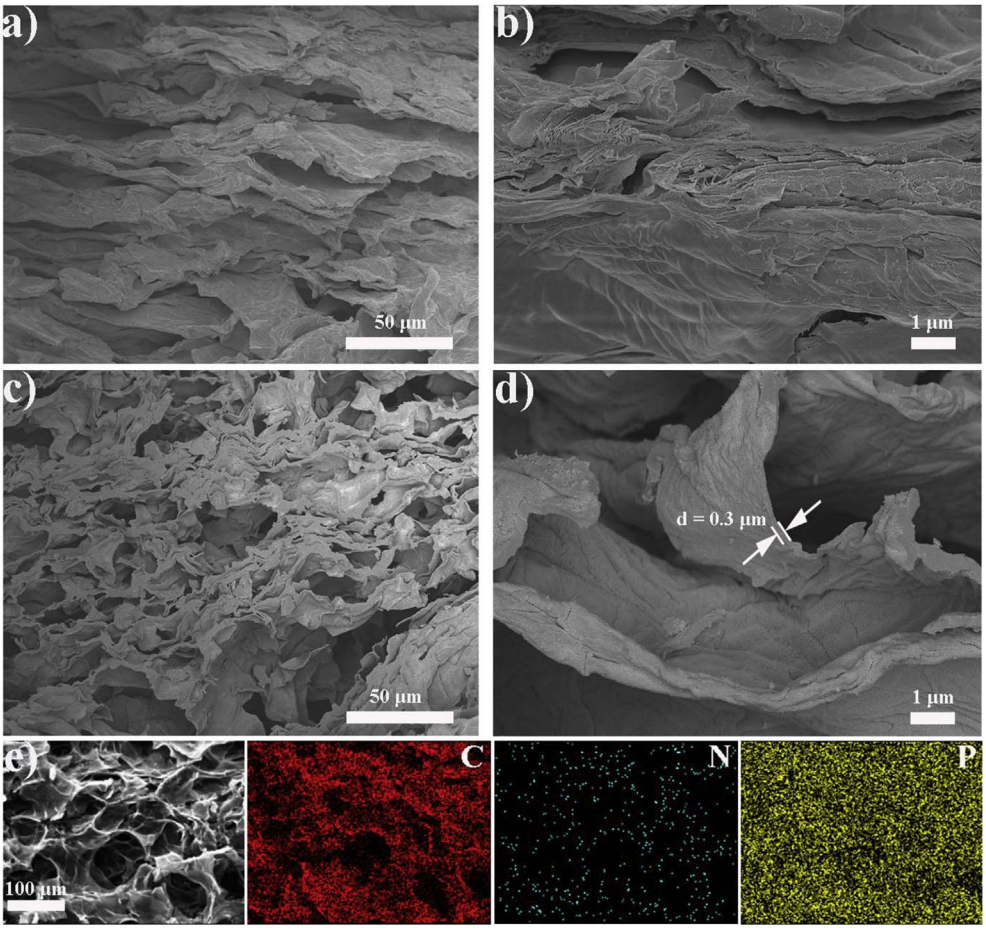

Fig. 2. SEM images of a and b) PP precursor, and c and d) PPC900-N&P30, and e) elemental mapping images for C, N, and P elements.

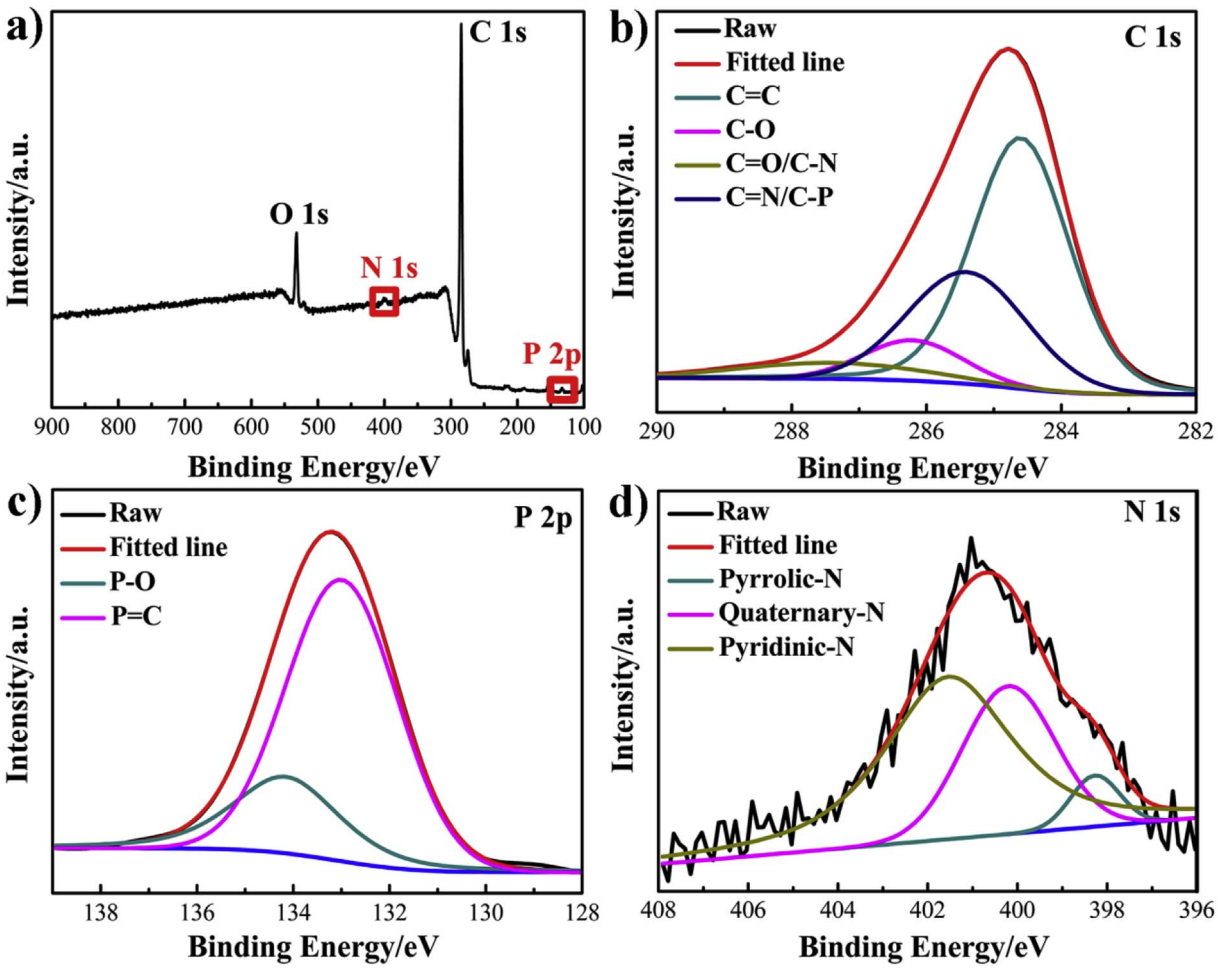

Fig. 3. XPS data of PPC900-N&P: a) full spectrum, and b-d) the curve fittings of C 1s, P 2p, and N 1s core level peak.

corresponded to C 1s, N 1s, P 2p, and O 1s, respectively. The curve fitting of C 1s core level peak of the XPS spectrum was divided into four main peaks, including C=C (284.5 eV), C-O (286.4 eV), C-N/C=O (287.4 eV) and C=N/C-P (285.4 eV) bonds [48,49], respectively (Fig. 3b). As shown in Fig. 3c, the curve fitting of P 2p core level peak was divided into two main peaks, including P-C (133.1 eV) and P-O (134.1 eV) on the surface of the sample [49,50]. Additionally, three nitride species occurred in the N 1s spectra (Fig. 3d), including pyrrolic-N (399.3 eV), quaternary-N (400.2 eV), and pyridinic-N (401.9 eV) [36], the quaternary-N was conducive to the electrons conduction, and thus improved the conductivity of carbon materials [51]. There were two main fitted peaks in the O 1s spectra (Fig. S5 in the Supporting Information) positioned at 531.6 and 533.0 eV, which respectively represented C=O and C-O bonds [52]. These results provided the definite evidence that P and N atoms were incorporated into the carbon framework, which was consistent with the result obtained from the SEM elemental mapping images. It is reported that incorporating heterogeneous atoms such as N and P would provide electrochemically active sites, enhance the wettability of an electrolyte on the electrode surface, and therefore improved the electrochemical performance [53,54].

Porosity structure of the samples was characterized by the TEM and BET method, and the results were shown in Fig. 4 and Fig. S4 in the Supporting Information. PPC900-N&P exhibited a mesoporous structure with the uniform pore size of 2–3 nm (Fig. 4a). It is reasonable that the activation process with DHP played a vital role in fabricating the porous structure, and the SAED (the inset in Fig. 4a) exhibited low crystallinity of activated carbon material. All PPC samples except PPC900 showed typical type III N_2 adsorption isotherm close to the X-axis at low relative pressures according to IUPAC classification, indicating a low specific surface area, and the N_2 molecules demonstrated a poor interaction with carbon materials (Fig. S4 in the Supporting Information). The pore structure parameters of PPCs samples were shown in Table 1. As can be seen, with the increase of carbonization temperature, the BET surface area (S_{BET}) and total pore volumes (V_{total}) of samples sharply increased from 0.694 to 627.5 m^2/g and from 0.0039 to 0.3552 cm^3/g, respectively, which could be attributed to the pyrolysis of biomass PP materials under carbonization process. CO and CO_2 were regarded as the most dominant gas products [37], and the carbonization eliminated some volatility organics and other carbon-containing low molecular weight substances [40,55]. The lignin of PP material had a wide temperature range (pyrolysis temperature ≥800 °C) [56], so the thermal decomposition reactions were more rapid, especially at elevated carbonization temperatures, thus resulting in more loose characteristics of the residual solid, which means that they demonstrate a large specific surface area. As shown in Fig. 4b, all the PPC900-N&Ps samples except PPC900-N&P5 presented standard type I N_2 adsorption isotherm close to the Y-axis at very low relative pressures and a nearly unchanged adsorption amount at higher relative pressures, indicating a narrow micropore size distribution [57], and the presence of micropores is beneficial in establishing the double layer, resulting in a higher specific capacitance of the material [58]. For PPC900-N&P5, there was no sufficient DHP participating in the activation, the porosity of the sample was quite undeveloped, which was similar to that of PPCs. Fig. 4c and d represent the N_2 adsorption isotherm and pore size distributions for PPC900-N&P30, there is rather high S_{BET} of about 807.7 m^2/g and a large V_{total} of 0.4378 cm^3/g. In

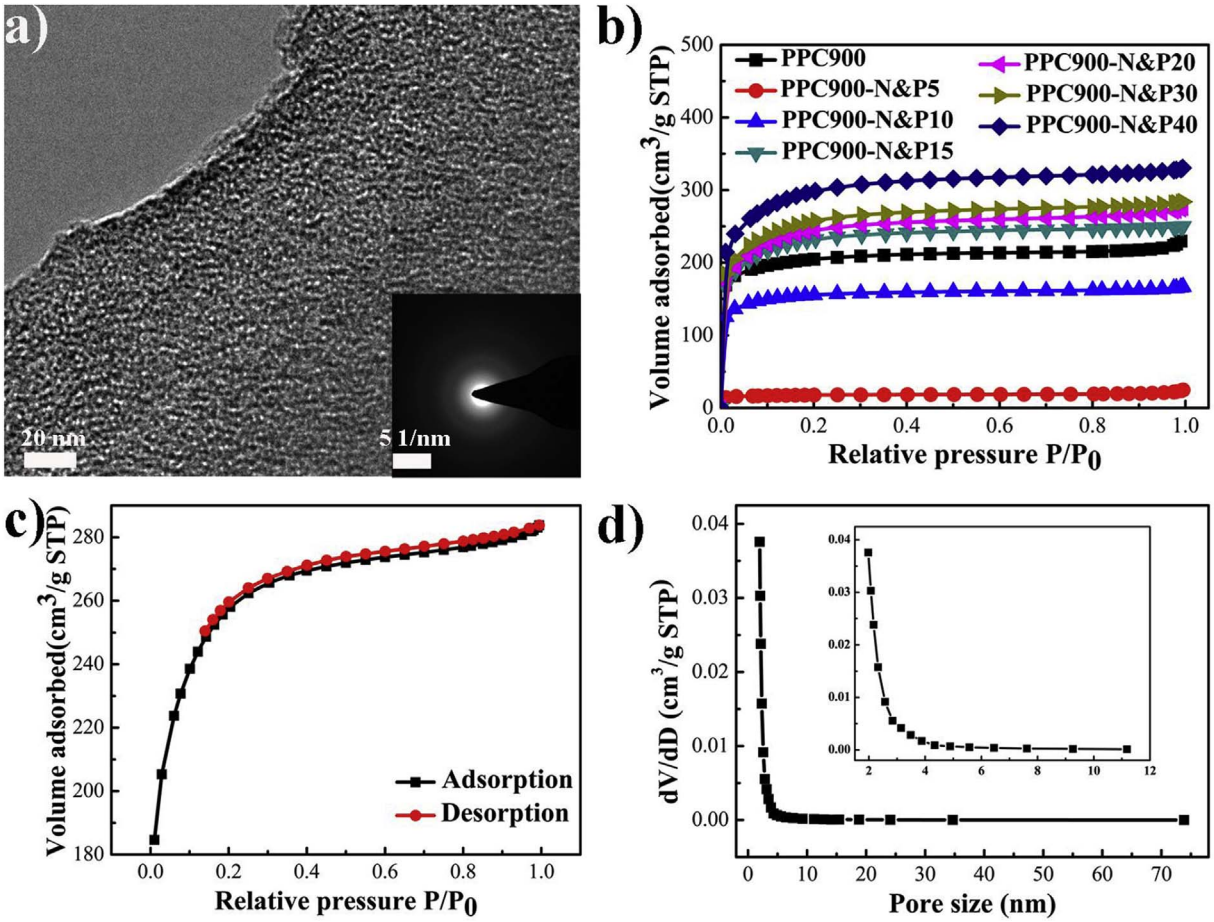

Fig. 4. Porosity characterization of PPC-N&Ps: a) TEM images (inset is the SAED pattern) of PPC900-N&P, b and c) nitrogen adsorption and desorption isotherms, and d) pore size distribution.

Table 1
Pore structure parameters of the different samples.

Sample	S_{BET} (m^2/g)	S_{mic} (m^2/g)	V_{total} (cm^3/g)	V_{mic} (cm^3/g)	d (nm)
PPC700	0.694	0.544	0.0039	0.0003	22.4
PPC800	2.004	1.604	0.0057	0.0005	11.3
PPC900	627.5	444.7	0.3552	0.2364	2.26
PPC900-N&P5	53.23	36.84	0.0365	0.0197	2.69
PPC900-N&P10	475.1	350.9	0.2567	0.1858	2.16
PPC900-N&P15	723.6	431.8	0.3865	0.2301	2.13
PPC900-N&P20	768.7	416.5	0.4343	0.2229	2.20
PPC900-N&P30	807.7	442.8	0.4378	0.2376	2.16
PPC900-N&P40	935.0	463.0	0.5085	0.2537	2.17

addition, it could be seen in Table 1 that the S_{BET} and V_{total} of DHP-incorporated activated carbon samples (PPC900-N&P5 and PPC900-N&P10) was lower than PPC900, indicating that a small amount of DHP could effectively improve the carbon yield, but obviously reduce the specific surface area of the carbon material. Remarkably, with the increase of DHP concentration, the S_{BET} and V_{total} value gradually increased, even higher than that of PPC900. As the DHP dosage increased, more potential sites could be penetrated and occupied by the activating agent, which benefited the following pore-opening and widening processes [59], thus resulting in a much more developed porosity. The pore size distribution was further calculated by the BJH method using the adsorption branch of the isotherm, further confirming the existence of micropore size of about 2 nm, which was consistent with the TEM result. The unique porous nanostructure was convenient for diffusion and transfer of electrolyte ions during the charging-discharging process [60]. Consequently, the electrochemical performance would be improved greatly.

The electrochemical performance of the electrodes prepared with PPC or PPC900-N&Ps was conducted in a three-electrode system using 2 M KOH aqueous as the electrolyte as shown in Fig. 5. All CV curves of PPC900-N&Ps electrodes presented nearly rectangular-like shapes, indicating an ideal double layer capacitive behavior of carbon (Fig. 5a). One can find that the surrounding area in the CV curve for PPC900-N&P30 electrode was the highest one compared with those of other samples, illustrating the highest specific capacitance of PPC900-N&P30. As shown in Fig. 5b, all GCD curves at 0.5 A/g were closely linear, and exhibited a symmetrical triangular shape with small IR drops, which suggested excellent columbic efficiency and a low resistance. The calculated specific capacitances of PPC900-N&P5, PPC900-N&P10, PPC900-N&P15, PPC900-N&P20, PPC900-N&P30, and PPC900-N&P40 were shown in Fig. 5d. The specific capacitance of PPC900-N&Ps increased and then decreased with the increase of DHP dosage, the specific capacitance values were 117, 156, 178, 188, 240, and 150 F/g, respectively (The C_{Vol} were 24.0 F/cm^3, 26.0 F/cm^3, 24.8 F/cm^3, 31.2 F/cm^3, 35.6 F/cm^3, 39.6 F/cm^3, 48.0 F/$cm^3$and 27.2 F/cm^3), respectively. The detailed data is shown in Table S2 in the Supporting Information, the volumetric capacitance of PPC900-N&P30 was higher than those of other PPC900-N&Ps and PPCs electrodes (the electrochemical performance of PPCs see Fig. S1 in supporting information), and comparable to the most previously reported carbon materials in the

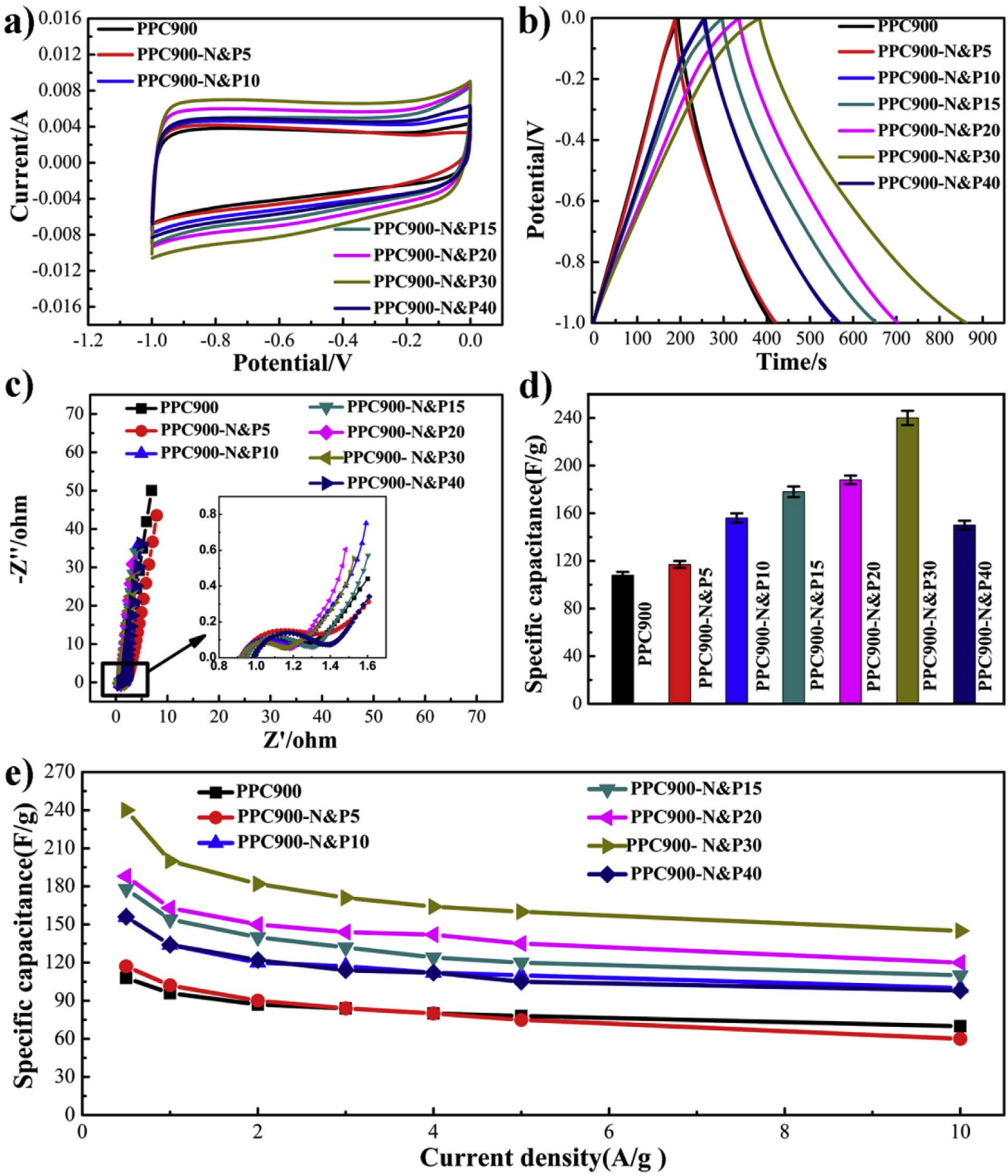

Fig. 5. Electrochemical performance tested by a three-electrode system: a) CV curves at 10 mV/s, b) GCD curves at 0.5 A/g, c) Nyquist plots, d) the specific capacitances at 0.5 A/g and e) the specific capacitances at different current density.

aqueous electrolytes (Table 2). Interestingly, PPC900-N&P30 had lower specific surface area (807.7 m^2/g) than that of PPC900-N&P40 (935.0 m^2/g) but showed higher specific capacitance. Although the specific surface area was an important parameter for the performance of electrochemical capacitors, it was sometimes not directly proportional to the specific surface area. This is because not all pores in the electrode layer were necessarily accessible to electrolyte ions [3,4]. Here, the highly curved and tortuous inner pore surfaces give the microsheets a high specific surface area, but lead to a less effective charge accumulation of the pores by sterical limitation compared to planar one [61]. In addition, a higher specific surface area may increase the risk of decomposition of the electrolyte during the process of charging/discharging storage [62]. The electrochemical impedance spectroscopy (EIS) was tested, the ideal EIS for an electrical double-layer capacitor (EDLC) included a straight line with a slope of close to 45° at a high-middle frequency region and an almost vertical line at low frequency range [63]. However, a semicircle loop in the high frequency region has been found for the carbon-based EDLCs with both aqueous and

Table 2
Comparisons of the porosity structure and electrochemical performance of carbon materials derived from biomass precursors.

Carbon precursor	Activation method	S_{BET}	Gravimetric capacitance	Volumetric capacitance	Measurement condition	Ref
Fungi	Thermal	80 m^2/g	196 F/g	No report	6 M KOH 5 mV/s	[27]
Seaweed	Thermal	746 m^2/g	244 F/g	224.0 F/cm^3	6 M KOH 2 mV/s	[32]
Firwood	KOH	1064 m^2/g	180 F/g	No report	0.5 M H_2SO_4 10 mV/s	[33]
Banana peel	$Zn(NO_3)_2$	1650 m^2/g	206 F/g	No report	6 M KOH 1.0 A/g	[29]
Banana peel	Thermal + NH_3	1357 m^2/g	210 F/g	No report	6 M KOH 0.5 A/g	[30]
Grapefruit peel	KOH	1760 m^2/g	311 F/g	No report	1 M H_2SO_4 0.1 A/g	[34]
Pistachio shell	KOH	1096 m^2/g	120 F/g	No report	0.5 M H_2SO_4 10 mV/s	[28]
Cassava peel	KOH + CO_2	1352 m^2/g	153 F/g	142.0 F/cm^3	0.5M H_2SO_4	[31]
Banana fiber	$ZnCl_2$	1097 m^2/g	74 F/g	No report	1M Na_2SO_4 500 mA/g	[68]
Pomelo peel	**Thermal + DHP**	**807 m^2/g**	**240 F/g**	**48.0 F/cm^3**	**2 M KOH 0.5 A/g**	**This work**

nonaqueous electrolytes in many works [34–36], which are different from the classic EIS. Various theories have been proposed to explain the cause of this semicircle loop: Sun et al. [63] proposed an equivalent model, which proved that the semicircle was ascribed to the contact resistance and contact capacitance between particles of activate materials, and between the electrode and current collectors. Dsoke S. et al. [64] demonstrated that the semicircle was attributed to the porous structures of the electrode with complex network. In addition, Nian et al. [65] believed that the semicircle of pseudocapacity was due to the interfacial redox reactions of impurities and surface functional groups. As shown in Fig. 5c, all the EIS were similar, being composed of one semicircle at high frequency followed by a linear component at low frequency. In the high frequency region, the intercepts with the x-real axis was a intrinsic ohmic resistance (R_s), the semicircle shape represented the charge-transfer resistance (R_{ct}), the presence of R_{ct} at high frequencies is mainly due to electrode porosity, and the interfacial resistance between current collector and electrode, and inter-particle contact resistance. In the low frequency region of the Nyquist plots was the Warburg diffusion resistance (R_w). The PPC900-N&P30 electrode exhibited smaller R_{ct} and R_s than those of the other PPC900-N&Ps electrodes. Compared to the others, PPC900-N&P30 electrode also displayed a vertical slope in the low frequency region, indicating a lower R_w at electrode/electrolyte interface. Fig. 5e showed the rate performances of PPC900-N&Ps and PPC900 electrodes demonstrated that the specific capacitance remained about 65% of initial specific capacitance when the current density increased from 0.5 to 10 A/g.

The electrochemical performance of PPC900-N&P30 was shown in Fig. 6. For all CV curves, with the typical characteristic of electrical double-layer capacitors, the current increased steadily in the potential window from −0.3 to −1 V, resulting from much more micropores being used for energy storage at enhanced voltages [66]. And the shape of CV curves at different scan rates showed no obvious change even at scan rate as high as 100 mV/s, indicating an ideal capacitive behavior of the electrode materials (Fig. 6a). In addition, all GCD curves of PPC900-N&P30 electrode at different current densities showed linear and symmetric triangular shapes, indicating excellent columbic efficiency and good electrochemical reversibility during the process of charging/discharging storage (Fig. 6b). The calculated specific capacitance of the electrode material was 240 F/g at the current density of 0.5 A/g. Fig. 6c showed the specific capacitance retention of the PPC900-N&P30 electrode. It could be seen that excellent cycling stability demonstrated approximately 100% capacitance retention after 10,000 cycles at the current density of 2 A/g, and the almost identical GCD curves for both the first cycle and the 10,000th cycle also indicated the excellent cycling stability (inset in Fig. 6c). The detailed electrochemical performance like CV and GCD curves for the various PPCs and PPC900-N&Ps electrodes are also shown in Fig. S6 and Fig. S7 in the Supporting Information. In addition, as shown in Fig. 6d, the Nyquist plot of PPC900-N&P30 electrode was almost vertical at the low-frequency region, and a segment of a semicircle at the high-frequencies, indicating the PPC900-N&P30 electrode had excellent wettability and ideal capacitive behavior. To obtain more information about the electrochemical behavior of the electrodes, an equivalent electrical circuit model was established [67] (inset in Fig. 6d). The fitted parameters for EIS obtained by Zswinpwin software of different samples were shown in Table 3, which was consistent with the results from the electrochemical impedance spectroscopy (EIS) measurements.

A symmetric electrochemical capacitor (SSC) consisting of the same PPC900-N&P30 electrodes was constructed by using 1 M Na_2SO_4 aqueous solution as the electrolyte. According to equation (3), enhancing voltage can be employed to increase the energy density of the device [69]. Compared with acid and alkali electrolytes, the neutral electrolyte (such as Na_2SO_4 aqueous) had low H^+ and OH^- concentration and oxygenated surface functionalities on the carbon surface resulting in high over-potential for dihydrogen evolution for carbon-based symmetric electrochemical capacitors [70]. The electrochemical performance of the device was shown in Fig. 7. CV curves of the SSC at different scan rates with potential windows ranging from 0 to 1.6 V displayed a quasi-rectangular shape even at a high scan rate of 200 mV/s, indicating an ideal capacitive behavior of carbon materials (Fig. 7a). The GCD curves showed symmetric triangular shapes and low IR drops, indicating excellent columbic efficiency and a low internal series resistance, the maximum specific capacitance value calculated from the GCD curve was 32 F/g at 0.2 A/g (Fig. 7b). Approximately 70% of the initial specific capacitance remained when the current density increased from 0.2 to 3 A/g (Fig. 7c). The EIS measurement was shown in Fig. 7d, the value of R_s calculated from the equivalent circuit model was as small as 4.16 Ω, indicating a common purely resistive response at high frequencies represented by the ohmic resistance of the electrode and electrolyte. Furthermore, the SSC showed excellent cycling stability with 99% capacitance retention after 10,000 cycles at 1 A/g (Fig. 7e). The CV curves had almost no significant change before and after 10,000

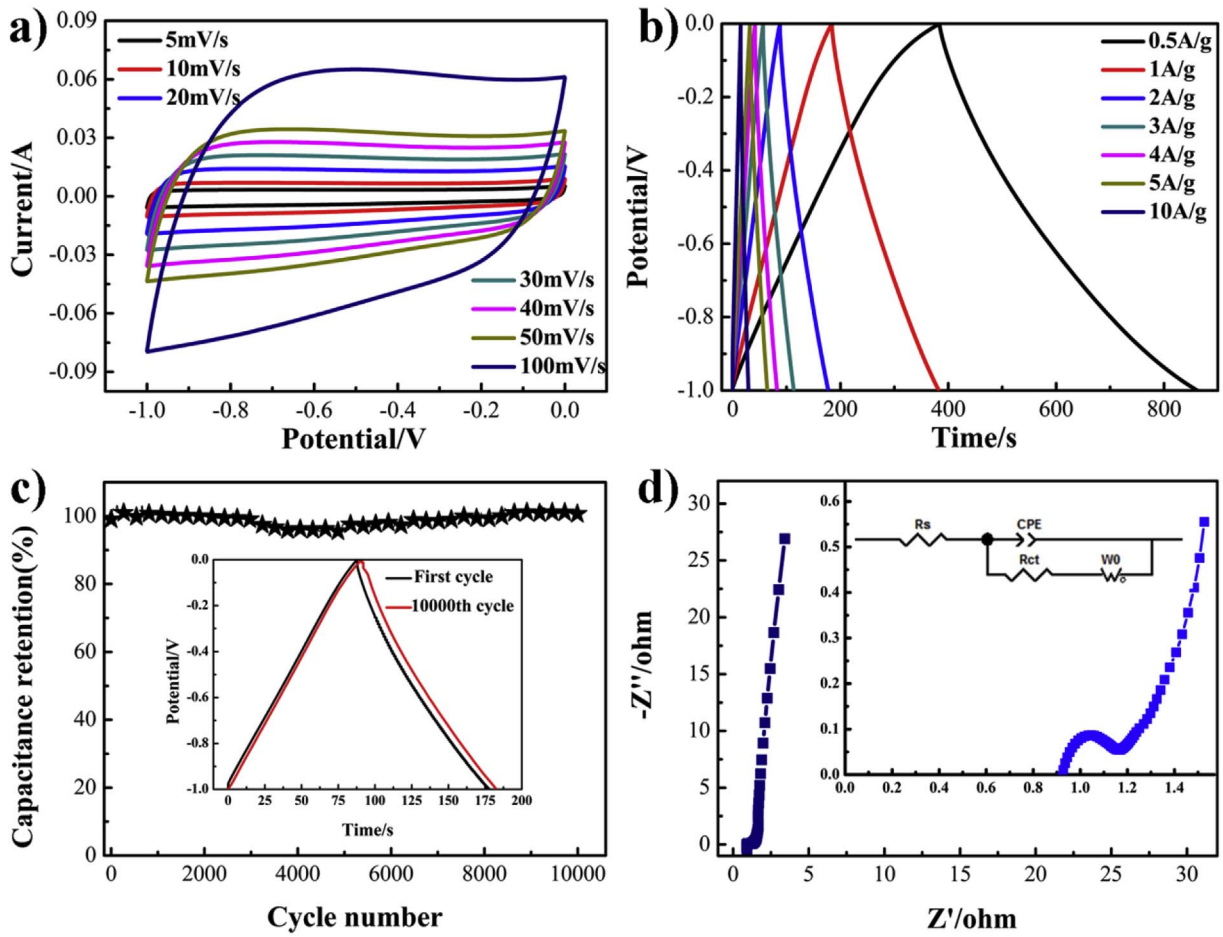

Fig. 6. Electrochemical performance of PPC900-N&P30: a) CV curves, b) GCD curves, c) the cycling stability at 2 A/g (the inset shows GCD curves of the first cycle and the 10000th cycle), d) Nyquist plot (the inset reveal the high-frequency region of the plot and the equivalent electrical circuit model).

Table 3
Fitted parameters for EIS obtained by Zswinpwin software of different samples.

Sample	R_S (Ω)	R_{CT} (Ω)	R_w (Ω)
PPC700	1.01	0.40	0.063
PPC800	0.86	0.30	0.049
PPC900	0.98	0.20	0.036
PPC900-N&P5	0.93	0.40	0.068
PPC900-N&P10	0.91	0.30	0.038
PPC900-N&P15	0.95	0.30	0.036
PPC900-N&P20	0.93	0.30	0.032
PPC900-N&P30	0.90	0.20	0.033
PPC900-N&P40	1.01	0.40	0.037
PPC900-N&P30||PPC900-N&P30 SSC	4.16	0.90	0.130

cycles at 10 mV/s (inset in Fig. 7e left), and the GCD curves still showed symmetric triangular shapes in the cycling test process (inset in Fig. 7e right), demonstrating excellent electrochemical cyclic stability. Energy density and power density were two important parameters for the evaluation of the device, and the Ragone plot of SSC (inset in Fig. 7c) was calculated, the cell showed a high energy density of 11.7 Wh/kg when the power density was 160 W/kg at a discharging current density of 0.2 A/g.

4. Conclusions

In summary, the porous layer-stacking carbon microsheets were synthesized through DHP impregnation treatment of pomelo peel and subsequent carbonization process. The carbon yield of DHP-treated PP was higher than that of untreated PP derived carbon. Remarkably, the as-obtained carbon material had a high surface area, narrow pore size distribution, and hierarchically interconnected thin microsheets framework. The nitrogen and phosphorus atoms were efficiently doped in the carbon material framework. Therefore, the carbon material exhibited good electrochemical behaviors, such as excellent cyclic stability, low resistance, and high specific capacitance. When the mass fraction of DHP was 30%, the prepared carbon material exhibited the best electrochemical performances, the specific capacitance of PPC-N&P30 had a maximum value of 240 F/g at the current density of 0.5 A/g, and superior cycling performance with the capacitance retention approximately 100% after 10,000 cycles at 2 A/g in 2 M KOH aqueous electrolyte. Furthermore, the assembled symmetric electrochemical capacitor in 1 M Na_2SO_4 aqueous electrolyte exhibited a high energy density of 11.7 Wh/kg at a power density of 160 W/kg, and excellent cycling stability with 99% capacitance retention after 10,000 cycles at 1 A/g. These exciting results suggest a low-cost and environmentally friendly design route for carbon material with the attractive electrochemical properties, which have a great potential for real application in energy storage.

Acknowledgments

This work was partly supported by the National Natural Science Foundation of China (51203071, 51463012, and 51763014), China Postdoctoral Science Foundation (2014M552509, and 2015T81064), Natural Science Funds of the Gansu Province (1506RJZA098), the

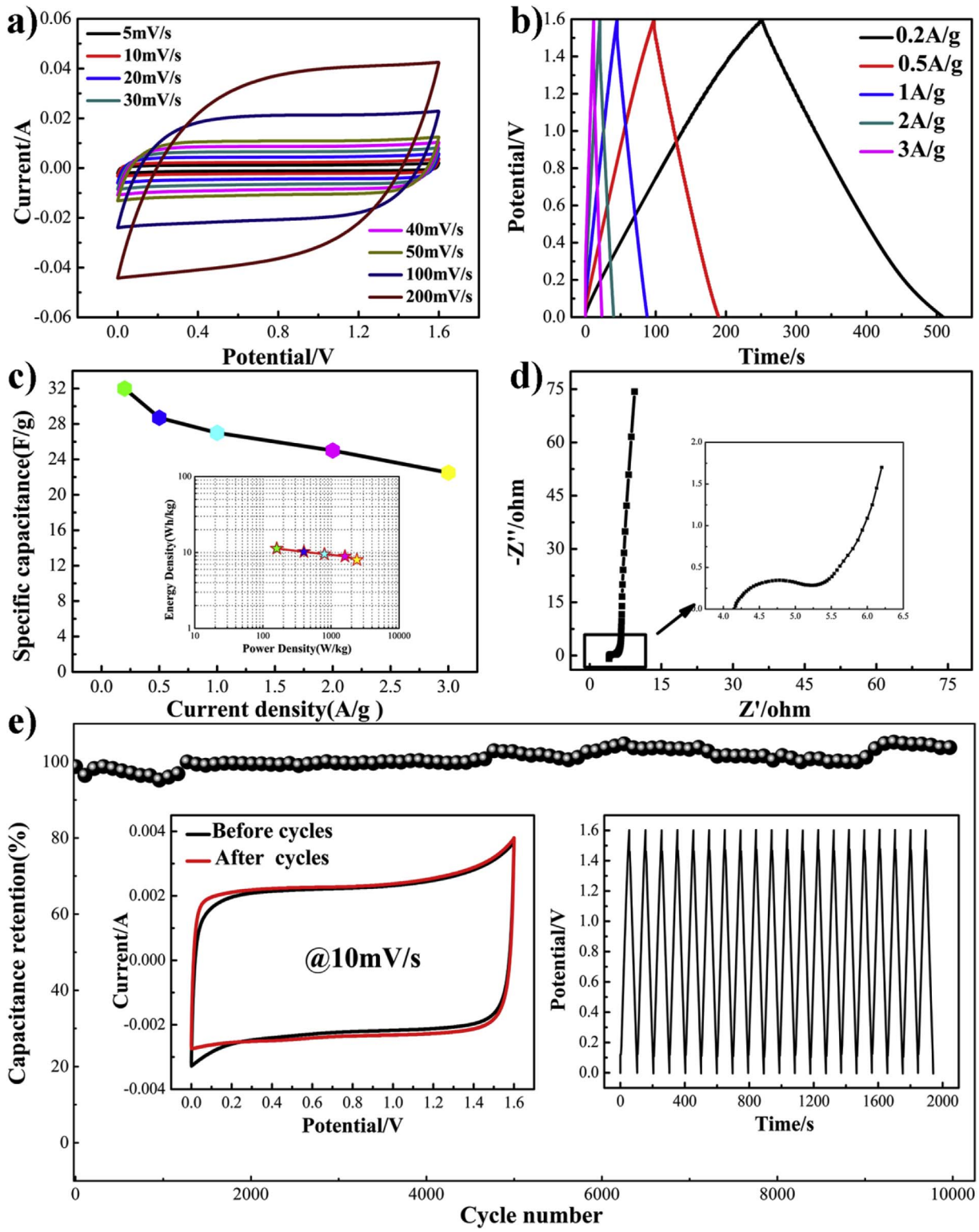

Fig. 7. Electrochemical performance for the SSC device assembled with PPC900-N&P30: a) CV curves, b) GCD curves, c) the specific capacitances at different current density (the inset shows Ragone plot), d) Nyquist plot, e) the cycling stability at 1 A/g (the inset show CV curves before and after 10,000 cycles at 10 mV/s and the GCD curves).

Program for Hongliu Distinguished Young Scholars in Lanzhou University of Technology (J201402), and the Opening Foundation of State Key Laboratory of Advanced Processing and Recycling of Non-Ferrous Metals (SKLAB02015001).

Appendix A. Supplementary data

Supplementary data related to this article can be found at http://dx.doi.org/10.1016/j.jpowsour.2017.12.076.

References

[1] P. Simon, Y. Gogotsi, Materials for electrochemical capacitors, Nat. Mater. 7 (11) (2008) 845–854.
[2] J.R. Miller, P. Simon, Electrochemical capacitors for energy management, Sci. Mag. 321 (5889) (2008) 651–652.
[3] G.P. Wang, L. Zhang, J.J. Zhang, A review of electrode materials for electrochemical supercapacitors, Chem. Soc. Rev. 41 (2) (2012) 797–828.
[4] L.L. Zhang, X.S. Zhao, Carbon-based materials as supercapacitor electrodes, Chem. Soc. Rev. 38 (9) (2009) 2520–2531.
[5] S.M. Aqeel, Z.Y. Huang, J. Walton, C. Baker, D. Falkner, Z. Liu, et al., Polyvinylidene fluoride (PVDF)/polyacrylonitrile (PAN)/carbon nanotube nanocomposites for energy storage and conversion, Adv. Compos. Hybrid Mater. (2017), http://dx.doi.org/10.1007/s42114-017-0002-5.
[6] Y.G. Wu, F. Ran, Vanadium nitride quantum dot/nitrogen-doped microporous carbon nanofibers electrode for high-performance supercapacitors, J. Power Sources 344 (2017) 1–10.
[7] A.K. Singh, D. Sarkar, K. Karmakar, K. Mandal, G.G. Khan, High-performance supercapacitor electrode based on cobalt oxide-manganese dioxide-nickel oxide ternary 1D hybrid nanotubes, ACS Appl. Mater. Interfac. 8 (32) (2016) 20786–20792.
[8] T. Liu, L. Finn, M. Yu, H. Wang, T. Zhai, X. Lu, et al., Polyaniline and polypyrrole pseudocapacitor electrodes with excellent cycling stability, Nano Lett. 14 (5) (2014) 2522–2527.
[9] G.A. Snook, P. Kao, A.S. Best, Conducting-polymer-based supercapacitor devices and electrodes, J. Power Sources 196 (1) (2011) 1–12.
[10] X.M. Lou, C.F. Lin, Q. Luo, J.B. Zhao, B. Wang, J.B. Li, et al., Crystal-structure modification enhanced $FeNb_{11}O_{29}$ anodes for lithium-ion batteries, Chemelectrochem (2017), http://dx.doi.org/10.1002/celc.201700816.
[11] L. Zhang, W. Yu, C. Han, J. Guo, Q.H. Zhang, H.Y. Xie, et al., Large scaled Synthesis of heterostructured electrospun TiO_2/SnO_2 nanofibers with an enhanced photocatalytic activity, J. Electrochem. Soc. 164 (9) (2017) H651–H656.
[12] Z.Y. Sun, L. Zhang, F. Dang, Y. Liu, Z.Y. Fei, Q. Shao, et al., Experimental and simulation understanding of morphology controlled barium titanate nanoparticles under co-adsorption of surfactants, Crystengcomm 19 (24) (2017) 3288–3298.
[13] C.B. Cheng, R.H. Fan, Z.Y. Wang, Q. Shao, X.K. Guo, P.T. Xie, et al., Tunable and weakly negative permittivity in carbon/silicon nitride composites with different carbonizing temperatures, Carbon (2017), http://dx.doi.org/10.1016/j.carbon.2017.09.037.
[14] C. Alippi, A unique timely moment for embedding intelligence in applications, CAAI Trans. Intell. Technol. 1 (1) (2016) 1–3.
[15] H.Y. Jin, Q. Chen, Z.X. Chen, Y. Hu, J.W. Zhang, Multi-leapmotion sensor based demonstration for robotic refine tabletop object manipulation task, CAAI Trans. Intell. Technol. 1 (1) (2016) 104–113.
[16] X.Y. Zhang, H.B. Gao, M. Guo, G.P. Li, Y.C. Liu, D.Y. Li, A study on key technologies of unmanned driving, CAAI Trans. Intell. Technol. 1 (1) (2016) 4–13.
[17] S. Padhy, S. Panda, A hybrid stochastic fractal search and pattern search technique based cascade PI-PD controller for automatic generation control of multi-source power systems in presence of plug in electric vehicles, CAAI Trans. Intell. Technol. 2 (1) (2017) 12–25.
[18] K. Sun, P.T. Xie, Z.Y. Wang, T.M. Sun, Q. Shao, Eun Ryu Jong, et al., Flexible polydimethylsiloxane/multi-walled carbon nanotubes membranous metacomposites with negative permittivity, Polymer 125 (2017) 50–57.
[19] Y.L. Ma, L. Lv, Y.R. Guo, Y.J. Fu, Q. Shao, T.T. Wu, et al., Porous lignin based poly (acrylic acid)/organo-montmorillonite nanocomposites: swelling behaviors and rapid removal of Pb (II) ions, Polymer 128 (2017) 12–23.
[20] K. Zhang, G.H. Li, L.M. Feng, N. Wang, J. Guo, K. Sun, et al., Ultralow percolation threshold and enhanced electromagnetic interference shielding in poly (l-lactide)/multi-walled carbon nanotube nanocomposites with electrically conductive segregated networks, J. Mater. Chem. C 5 (36) (2017) 9359–9369.
[21] J.N. Huang, Y.H. Cao, Q. Shao, X.F. Peng, Z.H. Guo, Magnetic nanocarbon adsorbents with enhanced hexavalent chromium removal: morphology dependence of fibrillar vs particulate structures, Ind. Eng. Chem. Res. 56 (38) (2017) 10689–10701.
[22] Z.J. Wu, S. Gao, L. Chen, D.W. Jiang, Q. Shao, B. Zhang, et al., Electrically insulated epoxy nanocomposites reinforced with synergistic core-shell SiO_2@MWCNTs and montmorillonite bifillers, Macromol. Chem. Phys. (2017), http://dx.doi.org/10.1002/macp.201700357.
[23] Y.J. Zheng, Y. Zheng, S. Yang, Z.H. Guo, T. Zhang, H.X. Song, et al., Esterification synthesis of ethyl oleate catalyzed by Bronsted acid-surfactant-combined ionic liquid, Green Chem. Lett. Rev. 10 (4) (2017) 202–209.
[24] Y.C. Li, X.L. Wu, J.F. Song, J.F. Li, Q. Shao, N. Cao, et al., Reparation of recycled acrylonitrile-butadiene-styrene by pyromellitic dianhydride: reparation performance evaluation and property analysis, Polymer 124 (2017) 41–47.
[25] C. Wang, Y.C. Wu, Y.C. Li, Q. Shao, X.R. Yan, C. Han, et al., Flame-retardant rigid polyurethane foam with a phosphorus-nitrogen single intumescent flame retardant, Polym. Adv. Technol. (2017), http://dx.doi.org/10.1002/pat.4105.
[26] W.Q. Yang, X.L. Wang, J.F. Li, X.R. Yan, S.S. Ge, S. Tadakamalla, et al., Polyoxymethylene/ethylene butylacrylate copolymer/ethylene-methyl acrylate-glycidyl methacrylate ternary blends, Polym. Eng. Sci. (2017), http://dx.doi.org/10.1002/pen.24675.
[27] H. Zhu, X.L. Wang, F. Yang, X.R. Yang, Promising carbons for supercapacitors derived from fungi, Adv. Mater. 23 (24) (2011) 2745–2748.
[28] F.C. Wu, R.L. Tseng, C.C. Hu, Comparisons of pore properties and adsorption performance of KOH-activated and steam-activated carbons, Microporous Mesoporous Mater. 80 (1) (2005) 95–106.
[29] Y.K. Lv, L.H. Gan, M.X. Liu, W. Xiong, Z.J. Xu, D.Z. Zhu, et al., A self-template synthesis of hierarchical porous carbon foams based on banana peel for supercapacitor electrodes, J. Power Sources 209 (209) (2012) 152–157.
[30] B.Z. Liu, L.L. Zhang, P.R. Qi, M.Y. Zhu, G. Wang, Y.Q. Ma, et al., Nitrogen-doped banana peel-derived porous carbon foam as binder-free electrode for supercapacitors, Nanomaterials 6 (1) (2016) 18.
[31] A.E. Ismanto, S. Wang, F.E. Soetaredjo, S. Ismadji, Preparation of capacitor's electrode from cassava peel waste, Bioresour. Technol. 101 (10) (2010) 3534–3540.
[32] M.P. Bichat, E. Raymundo-Piñero, F. Béguin, High voltage supercapacitor built with seaweed carbons in neutral aqueous electrolyte, Carbon 48 (15) (2010) 4351–4361.
[33] F.C. Wu, R.L. Tseng, C.C. Hu, C.C. Wang, Effects of pore structure and electrolyte on the capacitive characteristics of steam-and KOH-activated carbons for supercapacitors, J. Power Sources 144 (1) (2005) 302–309.
[34] Y.Y. Wang, B.H. Hou, H.Y. Lü, X.L. Wu, Hierarchically porous N-doped carbon nanosheets derived from grapefruit peels for high-performance supercapacitors, Chemistryselect 1 (7) (2016) 1441–1447.
[35] C. Peng, J.W. Lang, S. Xu, X.L. Wang, Oxygen-enriched activated carbons from pomelo peel in high energy density supercapacitors, RSC Adv. 4 (97) (2014) 54662–54667.
[36] G. Qu, S.F. Jia, H. Wang, F. Cao, L. Li, C. Qing, et al., Asymmetric supercapacitor based on porous N-doped carbon derived from pomelo peel and NiO arrays, ACS Appl. Mater. Interfac. 8 (32) (2016) 20822–20830.
[37] D.K. Shen, R. Xiao, S. Gu, K.H. Luo, The pyrolytic behavior of cellulose in lignocellulosic biomass: a review, RSC Adv. 1 (9) (2011) 1641–1660.
[38] D.K. Shen, S. Gu, Pyrolytic behaviour of cellulose in a fluidized bed reactor, Cellul. Chem. Technol. 44 (1) (2010) 79–87.
[39] G. Dobele, D. Meier, O. Faix, S. Radtke, G. Rossinskaja, G. Telysheva, Volatile products of catalytic flash pyrolysis of celluloses, J. Anal. Appl. Pyrol. 589 (2) (2001) 453–463.
[40] X. Zhou, P.L. Wang, Y.G. Zhang, X.M. Zhang, Y.F. Jiang, From waste cotton linter a renewable environment friendly biomass based carbon fibers preparation, ACS Sustain. Chem. Eng. 4 (10) (2016) 5585–5593.
[41] M. Statheropoulos, S.A. Kyriakou, Quantitative thermogravimetric-mass spectrometric analysis for monitoring the effects of fire retardants on cellulose pyrolysis, Anal. Chim. Acta 409 (1) (2000) 203–214.
[42] J. Gamby, P.L. Taberna, P. Simon, J.F. Fauvarquea, M. Chesneaub, Studies and characterisations of various activated carbons used for carbon/carbon supercapacitors, J. Power Sources 101 (1) (2001) 109–116.
[43] X. Li, J.P. Rong, B.Q. Wei, Electrochemical behavior of single-walled carbon nanotube supercapacitors under compressive stress, ACS Nano 4 (10) (2010) 6039–6049.
[44] D.W. Wang, F. Li, M. Liu, G.M. Lu, H.M. Cheng, 3D aperiodic hierarchical porous graphitic carbon material for high-rate electrochemical capacitive energy storage, Angew. Chem. Int. Ed. 47 (2) (2008) 373–376.
[45] Z.S. Wu, Y. Sun, Y.Z. Tan, S.B. Yang, X.L. Feng, K. Müllenet, Three-dimensional graphene-based macro-and mesoporous frameworks for high-performance electrochemical capacitive energy storage, J. Am. Chem. Soc. 134 (48) (2012) 19532–19535.
[46] A.C. Ferrari, J. Robertson, Resonant Raman spectroscopy of disordered, amorphous, and diamondlike carbon, Phys. Rev. B Condens. Matter 64 (7) (2001) 075414.
[47] M. Biswal, A. Banerjee, M. Deo, S. Ogale, From dead leaves to high energy density supercapacitors, Energy Environ. Sci. 6 (4) (2013) 1249–1259.
[48] Z. Lin, G. Waller, Y. Liu, M.L. Liu, C.P. Wong, Facile synthesis of nitrogen-doped graphene via pyrolysis of graphene oxide and urea, and its electrocatalytic activity toward the oxygen-reduction reaction, Adv. Energy Mater. 2 (7) (2012) 884–888.
[49] R. Li, Z.D. Wei, X.L. Gou, Nitrogen and phosphorus dual-doped graphene/carbon nanosheets as bifunctional electrocatalysts for oxygen reduction and evolution, ACS Catal. 5 (7) (2015) 4133–4142.
[50] D.S. Yang, D. Bhattacharjya, S. Inamdar, J. Park, J.S. Yu, Phosphorus-doped ordered mesoporous carbons with different lengths as efficient metal-free electrocatalysts for oxygen reduction reaction in alkaline media, J. Am. Chem. Soc. 134 (39) (2012) 16127–16130.
[51] J.J. Wu, D. Zhang, Y. Wang, B.R. Hou, Electrocatalytic activity of nitrogen-doped graphene synthesized via a one-pot hydrothermal process towards oxygen reduction reaction, J. Power Sources 227 (4) (2013) 185–190.
[52] L. Qie, W.M. Chen, H.H. Xu, X.Q. Xiong, Y. Jiang, F. Zuo, et al., Synthesis of functionalized 3D hierarchical porous carbon for high-performance supercapacitors, Energy Environ. Sci. 6 (8) (2013) 2497–2504.
[53] X. Yu, H.J. Kim, J.Y. Hong, Y.M. Jung, K.D. Kwon, J. Kong, et al., Elucidating surface redox charge storage of phosphorus-incorporated graphenes with hierarchical architectures, Nano Energy 15 (2015) 576–586.
[54] X.Y. Chen, C. Chen, Z.J. Zhang, D.H. Xie, X. Deng, J.W. Liu, Nitrogen-doped porous carbon for supercapacitor with long-term electrochemical stability, J. Power Sources 230 (15) (2013) 50–58.
[55] J. Deng, M.M. Li, Y. Wang, Biomass-derived carbon: synthesis and applications in energy storage and conversion, Green Chem. 18 (18) (2016) 4824–4854.
[56] T. Hosoya, H. Kawamoto, S. Saka, Cellulose-hemicellulose and cellulose-lignin interactions in wood pyrolysis at gasification temperature, J. Anal. Appl. Pyrol. 80 (1) (2007) 118–125.
[57] J. Zhou, Z.H. Li, W. Xing, H.L. Shen, X. Bi, T.T. Zhu, et al., A new approach to tuning carbon ultramicropore size at sub-angstrom level for maximizing specific capacitance and CO2 uptake, Adv. Funct. Mater. 26 (44) (2016) 7955–7964.
[58] Y.P. Zhai, Y.Q. Dou, D.Y. Zhao, S. Dai, Carbon materials for chemical capacitive energy storage, Adv. Mater. 23 (42) (2011) 4828–4850.
[59] Q.S. Liu, T. Zheng, P. Wang, L. Guo, Preparation and characterization of activated

carbon from bamboo by microwave-induced phosphoric acid activation, Ind. Crop. Prod. 31 (2) (2010) 233–238.
[60] T. Liu, K. Yu, L.N. Gao, H. Chen, N. Wang, L.H. Hao, et al., Graphene quantum dots decorated $SrRuO_3$ mesoporous film as an efficient counter electrode for high-performance dye-sensitized solar cells, J. Mater. Chem. A 5 (34) (2017) 17848–17855.
[61] C.L. Long, X. Chen, L.L. Jiang, L.J. Zhi, Z.J. Fan, Porous layer-stacking carbon derived from in-built template in biomass for high volumetric performance supercapacitors, Nano Energy 12 (2015) 141–151.
[62] E. Raymundo-Piñero, F. Leroux, F. Béguin, A high-performance carbon for supercapacitors obtained by carbonization of a seaweed biopolymer, Adv. Mater. 18 (14) (2006) 1877–1882.
[63] X.Z. Sun, B. Huang, X. Zhang, D.C. Zhang, H.T. Zhang, Y.W. Ma, Experimental investigation of electrochemical impedance spectroscopy of electrical double layer capacitor, Acta Physico-Chim. Sin. 30 (11) (2014) 2071–2076.
[64] S. Dsoke, X. Tian, C. Taubert, S. Schluter, Mehrens Wohlfahrt, Strategies to reduce the resistance sources on electrochemical double layer capacitor electrodes, J. Power Sources 238 (15) (2013) 422–429.
[65] Y.R. Nian, H. Teng, Influence of surface oxides on the impedance behavior of carbon-based electrochemical capacitors, J. Electroanal. Chem. 540 (2) (2003) 119–127.
[66] C. Vix-Guterl, E. Frackowiak, K. Jurewicz, M. Friebe, J. Parmentier, F. Béguind, Electrochemical energy storage in ordered porous carbon materials, Carbon 43 (6) (2005) 1293–1302.
[67] H.G. Wei, H.B. Gu, J. Guo, D.P. Cui, X.R. Yan, J.R. Liu, et al., Significantly enhanced energy density of magnetite/polypyrrole nanocomposite capacitors at high rates by low magnetic fields, Adv. Compos. Hybrid Mater. (2017), http://dx.doi.org/10.1007/s42114-017-0003-4.
[68] V. Subramanian, C. Luo, A.M. Stephan, K.S. Nahm, S. Thomaset, B.Q. Wei, Supercapacitors from activated carbon derived from banana fibers, J. Phys. Colloid Chem. C 111 (20) (2007) 7527–7531.
[69] Y.L. Yang, K.W. Shen, Y. Liu, Y.T. Tan, X.N. Zhao, J.Y. Wu, et al., Novel hybrid nanoparticles of vanadium nitride/porous carbon as an anode material for symmetrical supercapacitor, Nano-Micro Lett. 9 (1) (2017) 6.
[70] Q. Gao, L. Demarconnay, E. Raymundopiñero, F. Bequin, Exploring the large voltage range of carbon/carbon supercapacitors in aqueous lithium sulfate electrolyte, Energy Environ. Sci. 5 (11) (2012) 9611–9617.